Attenuation Structure of Coso Geothermal Area, California, from Wave Pulse Widths

by Huatao Wu and Jonathan M. Lees

Abstract   Pulse width data are used to invert for attenuation structure in the Coso geothermal area, California. The dataset consists of pulse width measurements of 838 microseismic events recorded on a seismic array of 16 downhole stations between August 1993 and March 1994. The quality factor Q correlates well with surface geology and surface heat flow observations. A broad region of low Q (≈ 30 to 37) is located at 0.5 to 1.2 km in depth below Devil's Kitchen, Nicol Prospects, and Coso Hot Springs. A vertical, low Q (≈ 36 in contrast with surrounding rock of 80) region is interpreted as a channel through which hydrothermal energy is transported from depth to the surface. The location of the channel is between stations S1 and S4, and its dimension is about 1 km. At the deep end of the channel, a large, broad body of low Q is also located at 3 km in depth 2 to 4 km to the southwest of Nicol Prospects and Devil's Kitchen. Since it lies at the bottom of the target region and beyond the scope of seismicity, further research is needed to constrain its extent. Numerical modeling with a pseudospectral method is also done to investigate the applicability of the inversion scheme to fractured regions. A linear relationship between pulse width broadening and travel time is upheld, and the proportional constants are estimated.

Introduction

The Coso, California, geothermal area is one of a series of geothermal resources along the eastern front of the Sierra Nevada range (Duffield *et al.*, 1980). The geological setting is tectonically complicated, as this region is in the transition zone between the right-slip San Andreas fault and the extensional Basin and Range Province (Roquemore, 1980). Magmatic intrusions are common in this region, as illustrated by maps of rhyolitic domes that dominate the topography of the Coso field (Fig. 1). Surface geology consists of Mesozoic basement rocks, late Cenozoic volcanic, and Quarternary alluvial deposits (Duffield and Bacon, 1981). The Quaternary rhyolitic domes were emplaced on Mesozoic bed rock in the last 1.02 million yr, and some very young volcanic rocks (0.044 to 0.055 m.y.) are associated with the highest observed heat flows and temperature gradients in the area (Combs, 1980). The regional stress field is northeast–southwest compression and southeast–northwest extension, controlling regional seismicity (Roquemore, 1980).

Extensive geological and geophysical investigations at Coso have been directed toward an accurate evaluation of the geothermal potential (Walter and Weaver, 1980; Reasenberg *et al.*, 1980). The geographic extent of the geothermal reservoir and the heat transport conduits from deep magmatic structures represent important parameters for the economic evaluation of the field. Useful indicators of rock property in regions of locally elevated temperature and pressure are the elastic wave velocity and attenuation. Generally, it is observed that velocity decreases and attenuation increases with increasing temperature (e.g., Suppe, 1985). In earlier studies, a broad, anomalous low-velocity region was isolated under the center of the Coso geothermal area at 10 to 17.5 km in depth using teleseismic travel-time residual analysis (Reasenberg, 1980). Furthermore, high attenuation has been observed in the top 5 km in the Coso–Indian Wells Valley region (Young and Ward, 1980; Ho-Liu *et al.*, 1988) using teleseismic and local seismic data. Walter and Weaver (1980) reviewed the regional seismicity of the Coso range and identified six seismic swarms, perhaps caused by dike injections. Aside from these clusters, it was noted that the seismicity was diffuse in the Coso region. However, resolution in these previous studies was limited by seismic signal frequency bandwidth, inversion block size, data coverage, and the availability of high-quality data. In this article, we present high-resolution attenuation structure for Coso using recently acquired, high-quality, microseismic data.

Observed seismic signals suggest that the quality quotient Q is roughly independent of frequency for a broad frequency band (Aki and Richards, 1980). Based on this, several methods have been developed to compute frequency-independent Q of intervening media (Tonn, 1989). The com-
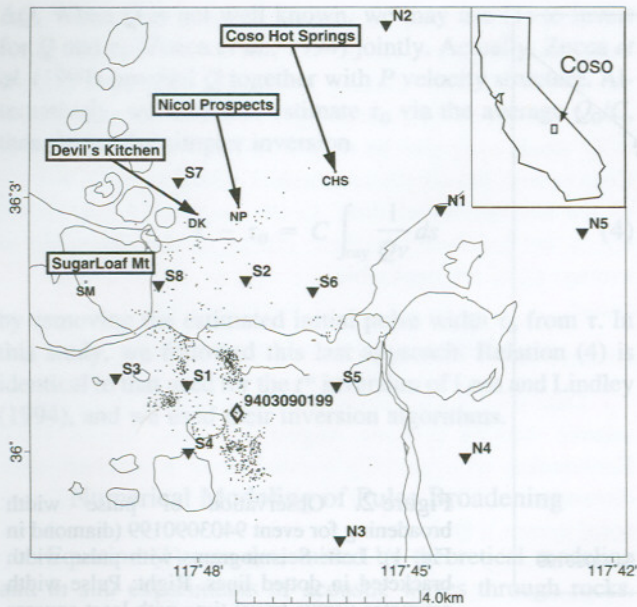
Figure 1. Geologic map of the geothermal field region at Coso, California. Highlighted circular features are rhyolitic domes. Small dots represent seismic events used in this study (diamond is event presented in Fig. 2), triangle symbols are seismic stations, and important geographic locations are annotated: DK, Devil's Kitchen; NP, Nicol Prospects; CHS, Coso Hot Spring; SM, Sugarloaf mountain.

monly used spectral ratio method, for example, compares the spectral content of two seismic signals that share the same source and provides a relative Q factor between two signals. The pulse width method (or rise time method), on the other hand, estimates the rate at which the signal reaches its peak, which depends on the frequency content, and thus can be associated with the amount of loss in the signal. Tonn (1989) compared seven methods for computing Q using synthetic data for a known velocity and Q model. No significant differences between methods were found for media that had some degree of heterogeneity.

Pulse width methods, like spectral ratio methods, do not require precise measurement of pulse amplitudes or instrumental response. Unlike spectral ratio methods, though, the pulse width methods only require a very short part of the first arriving signal, which is relatively free of other interfering waveforms (reflection, scattering, or multiple travel paths). In order to make accurate spectrum estimates, spectral ratio methods typically use 0.5 to 2 sec of data, whereas the pulse width may be estimated over half a wavelength of the *P*-wave arrival. Because of *P*-wave coda contamination, estimation of the slope of the log spectral ratio, which is needed to estimate Q for spectral methods, can contain a considerable amount of scatter (see Fig. 7 of Young and Ward, 1980). We thus use the pulse width method in this article to derive three-dimensional variations in Q.

The data were recorded on a permanent array of 16, three-component, downhole (typically 100 ft) seismometers deployed by Duke University and supported by the California Energy Co. and the U.S. Navy. Seismograms were recorded at 2-msec sampling with flat instrument response up to 100 Hz. The signals have high signal/noise (S/N) ratio, with S/N > 1 up to 90 Hz. The mean magnitude of the events used in this study is around $m_b = 0.5$ with hypocentral focus generally less than 5 km in depth. There is a sharp cutoff of seismicity at depths of approximately 3 to 4.7 km, although for shallower depths, seismicity is more or less evenly distributed in depth.

At Coso, pulse width broadening due to propagation is clearly observed. Figure 2 shows the first arriving *P* pulses recorded at various stations for an event in March 1994. The traces are arranged in the order of increasing travel times, and a systematic increase of pulse width with travel time is evident by visual inspection.

Pulse Broadening from Attenuation

Stacey *et al.* (1975) derived a formula for rise times of acoustic signals propagating linearly in elastic media with frequency-independent quality quotient (Q):

$$\tau = \tau_0 + C \int_{\text{ray}} \frac{ds}{vQ} = \tau_0 + C \int_{\text{ray}} \frac{dT}{Q}, \quad (1)$$

where τ is the pulse rise time, τ_0 is the original pulse rise time at the source, v is velocity, C is a constant, ds is an arc segment along ray path, and dT is the incremental travel time. The pulse rise time is defined as the amplitude of the first arriving pulse divided by the steepest rising slope. The rise time, defined on displacement records, is approximately the pulse width used by Zucca *et al.* (1994) on velocity seismograms. The pulse width, τ, is the time difference from onset of initial arrival to initial peak for displacement seismograms, or, equivalently, from onset to first zero crossing for velocity records or to second zero crossing for acceleration seismograms. In practice, the onset of a signal can be difficult to determine precisely in the presence of noise. Even for noise-free seismograms, bandwidth limitations can make picking the onset difficult. For short pulse widths, the error introduced by mispicking can be large and unacceptable. We follow Zucca's (1994) definition of pulse width with a slightly different measurement method: on the velocity seismograms, the time between the linear extrapolation of the rising slope at half peak to the time axis and the first zero crossing (Fig. 3) is used as the primary observation. Assuming a homogeneous $Q = Q_0$, equation (1) becomes a linear relation:

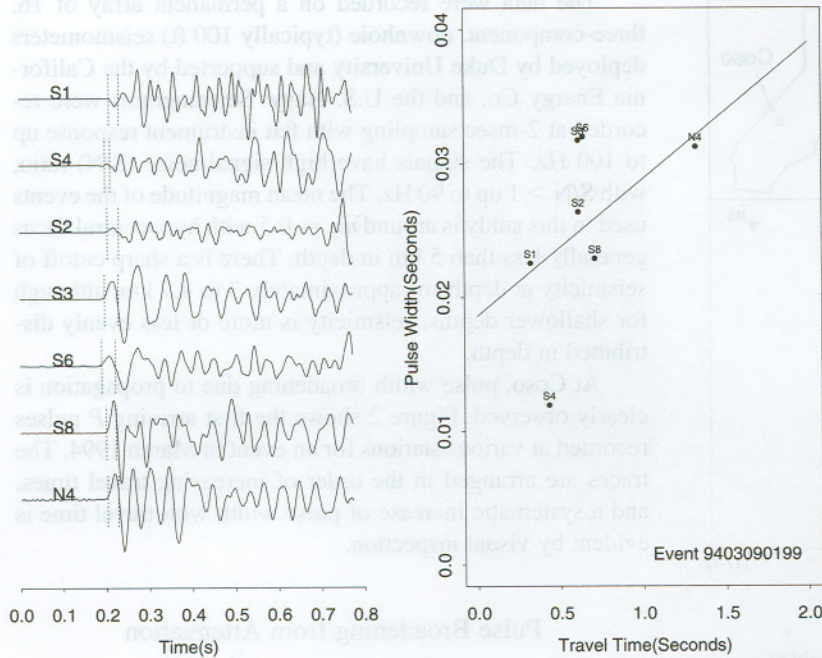$$\tau = \tau_0 + \frac{CT}{Q_0}. \quad (2)$$

Figure 2. Observation of pulse width broadening for event 9403090199 (diamond in Fig. 1). Left: Seismograms with pulse width bracketed in dotted lines. Right: Pulse width estimates versus travel time with least-squares fit. Note the broadening of first arrival pulses with travel time.
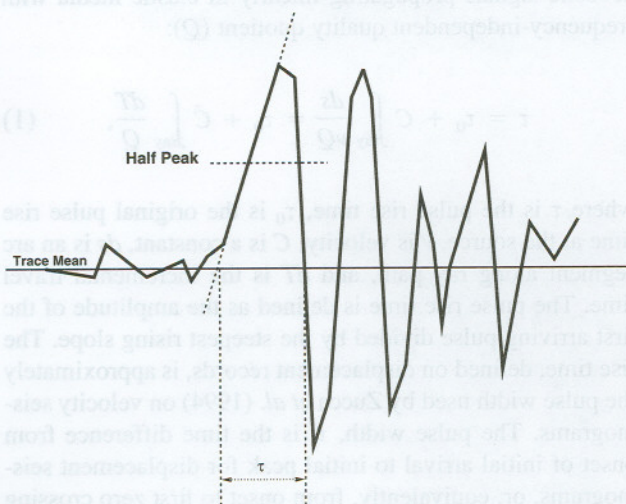

Figure 3. Definition of pulse width on velocity seismograms. Pulse width, τ, is measured between two zero crossings. The first is found by linear fit of the rising slope at half-peak, the second is the actual zero crossing of the zero-mean time series.

As an initial, albeit crude, approximation, the average Q_0/C can be estimated by a linear least-squares fit of pulse width data versus travel time.

The constant C in (1) was first determined experimentally (Gladwin and Stacey, 1974) for ultrasonic acoustic pulses in the kilohertz frequency band to be 0.5, and a rigorous theoretical justification was supplied later (Kjartansson, 1979). According to Kjartansson's (1979) theory of impulsive displacement sources, the rise time of recorded displacement, velocity, and acceleration traces each obey re-

lation (1), although with different constants C. For $Q > 30$, C will take on values of 0.485, 0.298, and 0.217 for displacement, velocity, and acceleration records, respectively (Blair and Spathis, 1982). Blair and Spathis (1982) further suggested that C can take on different values for different sources. Equation (1) should thus be applied only to signals from identical sources and should be calibrated on a per source basis by other, independent methods. For example, $C = 0.151$ for acceleration seismograms recorded in silica dolomite from a detonator source (Blair and Spathis, 1982).

Seismic sources are usually modeled as step dislocations on a fault plane. A forcing function that increases when rupture commences and decreases when rupture halts can be modeled as a step function source. In the far field, displacement is proportional to particle velocity on the fault plane at the source. A step dislocation source thus produces an impulsive displacement at the recording site. In the present study, where microseismic data is used, seismic sources are regarded as impulsive displacement sources. Since our data come as velocity seismograms, we adopt $C = 0.485 \approx 0.5$ based on theoretical results (Kjartansson, 1979). In fact, most of our interpretations remain valid without knowing the correct value of C: rather, we absorb the constant C into Q and invert for Q/C.

There are three approaches for setting up an inversion problem from equation (2). If the average Q model is reasonably well known, we let $Q = Q_0 + \Delta Q$,

$$\tau = \tau_0 + \frac{CT}{Q_0} - \frac{C}{Q_0^2} \int_{\text{ray}} \Delta Q \, dT \qquad (3)$$

and invert for both initial pulse width and/or perturbation

ΔQ. When Q is not well known, we may use (1) to invert for Q and τ_0 (Zucca *et al.*, 1994) jointly. Actually, Zucca *et al.* (1994) inverted Q together with P velocity structure. Alternatively, we may first estimate τ_0 via the average Q_0/C, then derive the simpler inversion

$$\tau - \tau_0 = C \int_{\text{ray}} \frac{1}{Qv} \, ds \qquad (4)$$

by removing the estimated initial pulse width τ_0 from τ. In this study, we followed this last approach. Relation (4) is identical to that used for the t^* inversion of Lees and Lindley (1994), and we used their inversion algorithms.

Numerical Modeling of Pulse Broadening

Equation (1) was determined by theoretical modeling and *in situ* experiments of acoustic waves through rocks. However, the frequency range used in laboratory experiments is considerably higher than that observed in typical seismic data. Furthermore, the theoretical derivation (Kjartansson, 1979) prescribes an idealized impulsive source in homogeneous media and, therefore, may only hold for non-realistic, infinite frequency sources. The empirical linearity of (1) for arbitrary sources has not been modeled theoretically (Blair and Spathis, 1982), and its applicability to real earthquake sources is unknown. Effects of heterogeneities introduce further complications that are also not well understood. In heavily fractured regions, like Coso, effects of cracks, partially molten rock, and hot fluids may be significant.

We would like to know if the presence of heterogeneities and cracks significantly alter our assumption of linearity. To test the linearity assumption, we devised synthetic models, including cracks, and used these to propagate synthetic waves with a pseudo-spectral (PS) method of seismic-wave simulation (Witte and Richards, 1990; Wu and Lees, 1994). An example two-dimensional model is presented in Figure 4 with a source offset from 16 surface stations. Since we do not have access to source functions, we experimented with several, including error functions, Gaussians, derivatives of Gaussians, and Ricker wavelets, each with a cutoff frequency of 20 Hz. A simple, attenuating, rheological model

with nearly constant Q within a frequency band 1 to 20 Hz is used to simulate seismic waves (Wu and Lees, 1994) through a heterogeneous model. In our experiments, we use a rheological scheme represented by a generalized Maxwell model with six Maxwell elements. The quality quotient, Q, of this model is ~25. The limiting $P(S)$ velocities of this model for frequency 0 (relaxed) and ∞ (unrelaxed) are 5.37 (2.73) and 6.10 (3.10) km/sec, respectively. An explosive source is used, and computation is performed on a 2D grid of 256 by 128 blocks with isotropic grid spacing of 0.1 km. The source is represented by four grid points with lateral extent of two grid blocks (0.2 km, Fig. 4).

The purpose of the synthetic modeling is to establish the linear relationship of equation (2) in the presence of heterogeneities, as represented by cracks in the model, and to determine an estimate for the constant C in equation (2). The synthetic seismograms represent particle velocity. For dipole sources, the step forcing generates impulsive displacement in the far field. Analogously, impulse forcing generates double-impulsive displacement in the far field. Thus, velocity seismograms for error functions are identical to displacement seismograms for Gaussian sources. We concern ourselves here only with vertical seismograms because pulse widths in our data are measured only on the vertical component. The main results of the tests are summarized in Table 1, and Figure 5 shows pulse width measurements for the four tested sources in a homogeneous model, plotted against travel time: linearity of pulse width versus travel time is unquestionable. If we introduce fractures into the model (Fig. 4), linearity is reasonable (Fig. 6) but not as perfect as in homogeneous models. Linearity is apparently mostly distorted for derivative Gaussian sources.

Table 1 shows that C depends on variations of source frequency content in the four test sources. Our numerical estimates of C are consistently larger than theoretical values, in part due to the fact that synthetic cases have lower-frequency content compared to any "compatible" sources. At low- and high-frequency ranges, Q is no longer constant for Generalized Maxwell models, and therefore, the discrepancy between numerical estimates and theory are magnified. A source is "compatible" with an impulse when its spectrum can be derived from an impulse spectrum via the attenuation filtering of propagation through a constant (or variable) Q model, i.e., by the application of a series of low-pass filters
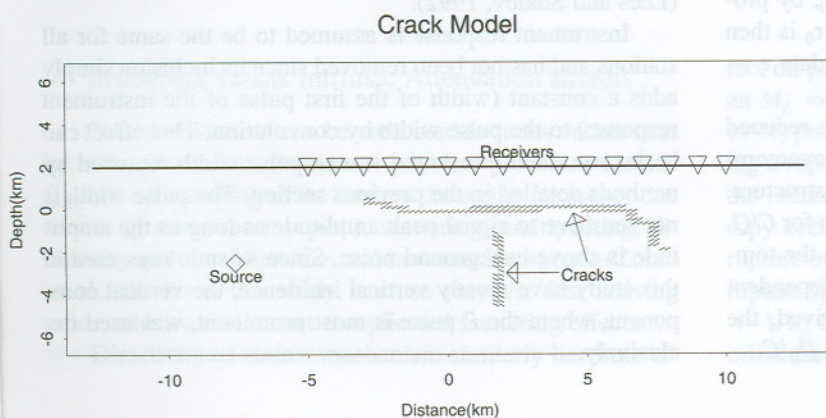

Crack Model

Figure 4. Two-dimensional, synthetic model used for wave simulation in heterogeneous media. The synthetic models is a vertical cross section spanning 20 km. Line segments represent crack direction and distribution, and diamond at lower left denotes the source position. Pseudo-spectral methods are used to propagate waves from the explosive source to 16 receivers at the surface.

Table 1
Numerical Slopees C/Q and C

| Source | Homogeneous | | Fractured | | Theory |
	Slope C/Q	C	Slope	C	C
Err Func	0.0322	0.805	0.0366	0.915	0.485
Gaussian	0.0148	0.370	0.0190	0.475	0.298
1st Gaussian	0.0092	0.231	0.0159	0.398	0.217
Ricker	0.0058	0.145	0.0035	0.087	—

in the form $\exp\left(-\dfrac{\pi f x}{vQ}\right)$ along the ray path (Gladwin and Stacey, 1974). This filter is 1 at $f = 0$, thus a source with zero energy at $f = 0$ can never be compatible with an impulse: there exists no frequency-independent attenuation process that can reduce power at $f = 0$ to zero without simultaneously reducing the whole spectrum to zero. We note that, of the four test sources used here, derivative Gaussian and Ricker wavelets are not compatible with impulsive sources. For a hypothetical source that resembles a low-pass filtered impulse, relation (1) holds with $C = 0.485$. First arrival velocity pulses at Coso (and probably for all microseismic earthquakes) appear closest in shape to derivative Gaussian pulses that correspond to Gaussian function displacements. Gaussian displacements, in turn, correspond to error function forcing at the source, which is in effect a step forcing function. We thus choose to use the theoretical value of C = 0.485 that corresponds to an impulse displacement function. Considering that the Gaussian has more low-frequency content than any compatible pulses, the real data inversion may require a larger C. A compromise between numerical and theoretical results suggests we use $C = 0.65$. Below, we discuss the use of both these choices in our analysis.

Inversion of Real Data

Each event has a different initial source pulse width and, in order to extract path-broadening effects, a source pulse width must be subtracted from measured pulse widths. By forming a linear regression of measured pulse widths against travel time, we obtain a quantity, Q_0/C, the average quality factor divided by C. Using C/Q_0 as the slope, we are able to fit the measured pulse width data for each event with a straight line and obtain the source pulse width, τ_0, by projecting the line to zero travel time. The intercept τ_0 is then removed from the measured data τ. The reduced data $\tau - \tau_0$ represents pulse broadening due to propagation.

After removing the source pulse width, some reduced data have unphysical negative values, arising from overcompensating path effects associated with attenuation structure. We use the reduced data to derive a linear inversion for C/Q. The linear fit estimating Q_0/C is not dependent on the tomographic inversion, but tomographic inversion is dependent on Q_0/C. After the tomographic inversion is derived, the average Q/C should agree with initial estimates of Q_0/C.

Errors in picking first arrival times do not affect measurements of pulse widths, as long as the correct initial pulses are selected. Picking errors will, however, slightly affect estimation of average Q_0/C. Picking errors are typically small compared to overall travel times, estimated at Coso to be 0.006 sec (three samples), which is less than 0.5% of the average travel time. Given such small travel-time errors, we conclude that these effects on the estimation of average Q_0/C are negligible.

Data Selection and Preparation

Data used in this study were recorded at 16 downhole seismic stations between August 1993 and March 1994. Earthquakes were initially located using a standard, one-dimensional (1D), layered model (Peter Malin, 1994, personal comm.). Only events located within the targeted volume including six or more P arrival readings were selected for analysis. About a quarter of the full data set falls within these criteria, yielding 838 events with 3134 usable traces.

Since velocity seismograms were used, pulse width, from the onset of the signal to the first zero crossing, was measured after removing the mean value of each seismogram (Fig. 2). Systematic measurement errors in pulse width may be absorbed either into the constant C or into source pulse width τ_0 and thus do not change estimates of relative Q. Pulse width data were initially measured automatically and later visually examined trace by trace for quality control. Where automatic methods failed, pulse widths were repicked by hand, and traces with complicated or abnormal initial pulses were discarded.

Station locations and travel-time corrections used in the inversion are shown in Table 2. The station corrections are determined from the residual analysis of earthquake locations and correlate well with topography. The 3D velocity model we use in our Q inversion is derived through an independent linear inversion using a much larger data set (Lees, 1995, unpublished results). There is a broad, high-velocity anomaly in the northwestern part of the target region at 0.5 to 2.44 km in depth, and low-velocity zones are found in the eastern and southeastern regions. The three-dimensional velocity features are very smooth, and earthquake locations relative to the three-dimensional models are not significantly different from one-dimensional locations (Lees and Shalev, 1992).

Instrument response is assumed to be the same for all stations and has not been removed since its inclusion simply adds a constant (width of the first pulse of the instrument response) to the pulse width by convolution. This effect can be incorporated into initial source pulse width removed by methods detailed in the previous section. The pulse width is not sensitive to signal peak amplitude as long as the amplitude is above background noise. Since seismic rays used in this study have mostly vertical incidence, the vertical component, where the P pulse is most prominent, was used exclusively.
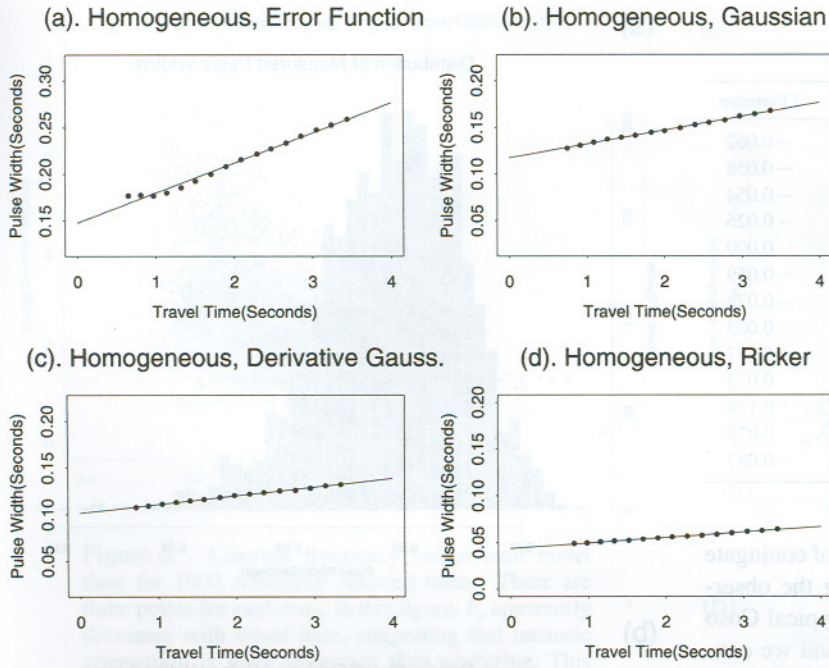
Figure 5. Pulse width versus travel time for homogeneous model with four synthetic sources. (a) Error function. (b) Gaussian function. (c) First derivative Gaussian. (d) Ricker wavelet. Deviations from linear fit represent anisotropic effects associated with finite source size.
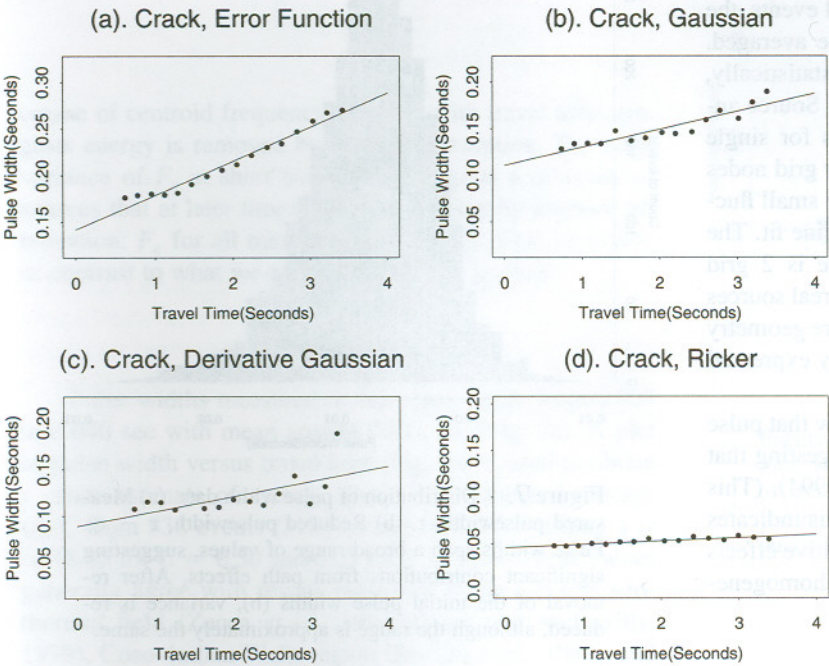

Figure 6. Same as Figure 5, but for heterogeneous crack model. (a) Error function. (b) Gaussian function. (c) First derivative Gaussian. (d) Ricker wavelet. The predicted linear trend persists, as in Figure 5, with the introduction of significant heterogeneity.

Scattering versus Intrinsic Attenuation Effects

Pulse broadening can be attributed to factors other than intrinsic absorption. Prominent physical processes include f_{max} effects (masking of the earthquake corner frequency due to low Q along the ray path), scattering, multipathing, directivity and size of source, and instrument response (Zucca et al., 1994). In this study, we use only the first arriving pulse, which avoids most complicated scattering effects.

Directivity of source mechanism similarly has little ef-

fect on pulse shape. For example, a Brune source model for an $M_L = 1.1$ earthquake has size of ~20 m (Zucca et al., 1994) producing a source signal of ~7.4 msec wide (assuming a rupture speed of 2.7 km/sec). Finite source size makes the initial pulse width anisotropic, where maximum anisotropy occurs in directions opposite that of the rupture. For a rupture of length L with seismic velocity $V_p = 6$ km/sec and rupture speed $V_R = 2.7$ km/sec, pulse width equals $L*(1/V_R + 1/V_p \cos \theta) = 7.4 + 3.3 \cos \theta$ msec, where θ is the orientation angle from the rupture direction. For double-

Table 2

Station Table

Station ID	Latitude	Longitude	P Correction	S Correcton
S1	36N00.7852	117W48.1522	−0.053	−0.062
S2	36N02.0210	117W47.3002	−0.050	−0.058
S3	36N00.8678	117W49.1894	−0.046	−0.054
S4	35N59.9878	117W48.1359	−0.023	−0.026
S5	36N00.7686	117W45.9964	0.000	0.000
S6	36N01.8911	117W46.3327	−0.051	−0.059
S7	36N03.1822	117W48.2752	−0.024	−0.028
S8	36N01.9631	117W48.5644	0.002	0.003
N1	36N02.8500	117W44.4766	−0.108	−0.187
N2	36N05.0333	117W45.2600	0.042	0.073
N3	35N58.9500	117W45.9500	0.068	0.118
N4	35N59.9300	117W44.1300	0.044	0.075
N5	36N02.5800	117W42.4200	−0.051	−0.087

(a)

(b)

Figure 7.   Distribution of pulse width data. (a) Measured pulsewidth, τ. (b) Reduced pulsewidth, $\tau - \tau_0$. Pulse widths span a broad range of values, suggesting significant contributions from path effects. After removal of the initial pulse widths (b), variance is reduced, although the range is approximately the same.

couple sources, θ is between 0 and $\pi/2$ (because of conjugate directions), so fluctuation of pulse width along the observation direction is $3.3 \times 0.707 = 2.3$ msec. Typical Coso sources ($m_b = 0.5$) are considerably smaller, and we conclude that effects of rupture size are not significant compared with average measured pulse width (21 msec). Furthermore, even if these effects are important for individual events, the random orientation of suites of ruptures will be averaged. Average rupture broadening, if not zeroed out statistically, is thus incorporated in the initial pulse width τ_0. Source anisotropy is observed on synthetic seismograms for single events using an explosive source applied at four grid nodes (Figs. 5 and 6). Anisotropic effects are noted by small fluctuations of pulse width around a linear straight line fit. The source size in the numerical modeling scheme is 2 grid nodes, or 0.2 km, which is much larger than the real sources used in our study, so we expect that source rupture geometry does not have a significant effect on the linearity expressed in equation (1).

Histograms of the full data set (Fig. 7a) show that pulse width data span the full pulse width range, suggesting that f_{max} effects are not pronounced (Zucca et al., 1994). (This effect is true for individual stations as well.) This indicates that measured attenuation (Q) represents the additive effects of intrinsic attenuation (Q_i) and scattering by inhomogeneities (Q_s), as

$$\frac{1}{Q} = \frac{1}{Q_i} + \frac{1}{Q_s}. \qquad (5)$$

Scattering tends to delay arrival of high-frequency energy while intrinsic absorption removes it from wave fields (Richards and Menke, 1983).

To investigate the relative importance of scattering and intrinsic attenuation, the centroid frequency is used to measure shifts of spectrum energy within P-wave trains. Centroid frequency F_c is defined as the frequency that evenly divides the total energy in the spectrum. Using a set of 1000 arbitrarily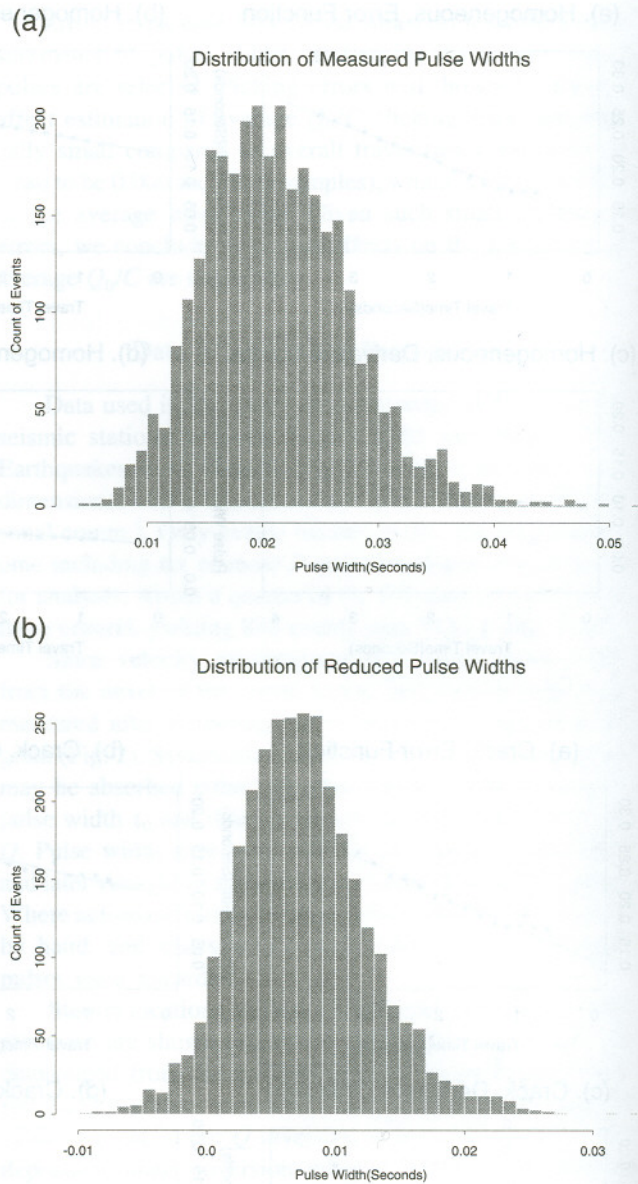 selected traces, centroid frequencies in spectral windows of 10 to 100 Hz were calculated in a series of three, 50% overlapping time windows (0.1 sec) from the onset of the P wave up to the onset of the S wave. The centroid frequency exhibited a general decrease with total travel time from origin to the window where F_c is computed (Fig. 8) and the apparent negative slope indicates the dominance of intrinsic absorption over scattering attenuation. While we show all 3000 (three windows for 1000 signals) points in Fig. 8, the trend of decreasing frequency content for each individual event is generally observed. Furthermore, the de-
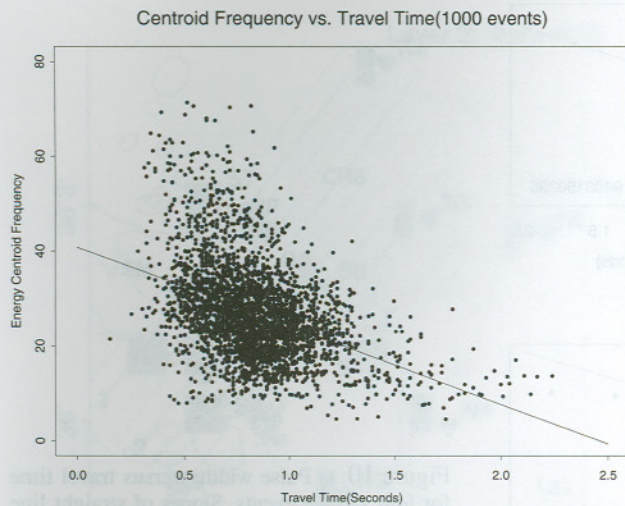
Centroid Frequency vs. Travel Time(1000 events)

(a)

Pulse Width vs. Travel Time(OutLiers Removed)

Figure 8. Centroid frequency versus total travel time for 1000 arbitrarily selected traces. There are three points for each trace in this figure. F_c apparently decreases with travel time, suggesting that intrinsic attenuation is more important than scattering. This trend is apparent on individual events as well. Straight line is least-squares fit for all 3000 points.

(b)

Corrected Pulse Width vs. Travel Time(OutLiers Removed)

crease of centroid frequency variance with travel time suggests energy is removed by intrinsic absorption. The large variance of F_c at short travel time suggests a diversity of sources that at later times are smoothed out by intrinsic attenuation: F_c for all traces tends to zero as time increases, in contrast to what we expect for scattering alone.

Estimates of Q

Pulse widths measured in this study range from 0.005 to 0.040 sec with mean around 0.021 sec (Fig. 7a). A plot of pulse width versus travel time (Fig. 9a) is used to obtain a crude estimate of average Q_0/C. The estimated average Q_0/C from 838 events (3134 traces) is 97.70, yielding a Q of 48.85 for $C = 0.50$ and 63.5 for $C = 0.65$. These values generally agree with results estimated at the Geysers geothermal field (Zucca *et al.,* 1994; Majer and McEnvilly, 1979), Coso–Indian Wells region (Ho-Liu *et al.,* 1988), and Coso (Young and Ward, 1980). The large variance of the linear fitting implies a deviation of Q from homogeneous Q_0. Measured pulse widths for individual events generally increase with travel time (Fig. 10). The average initial pulse width (0.014 sec) accounts for ~67% of the average measured pulse width (0.021 sec). We observed that source pulse width slightly decreases with depth. After removing the source pulse width, the reduced data set $\tau - \tau_0$ is used in Q inversion. The reduced data plotted against travel time (Fig. 9b) has variance slightly less than Figure 9a. This indicates that the original variance contains effects of irregularities of both initial pulse width and attenuation structure.
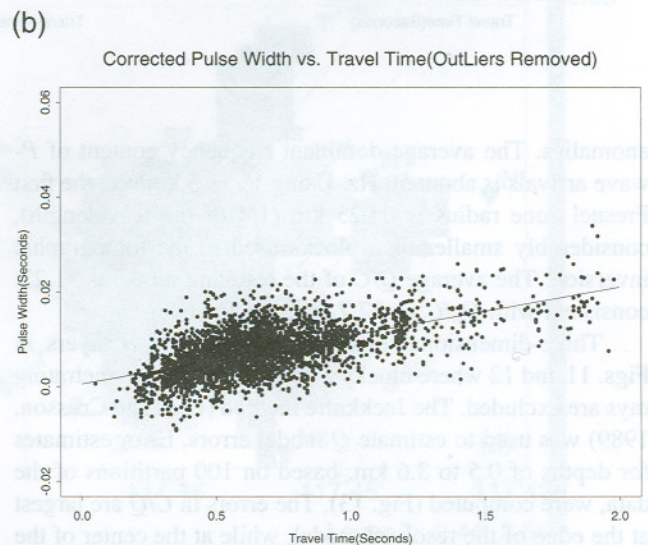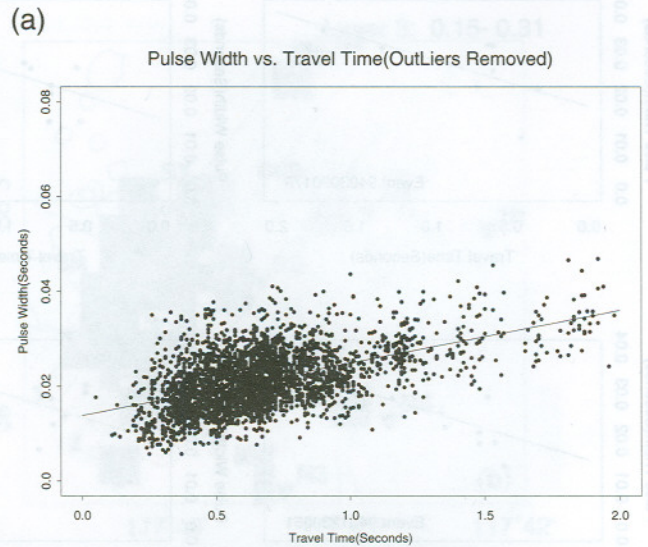
Figure 9. Scatter plot of pulse width versus travel time. (a) Raw τ measured from *P*-wave arrivals. Slope of straight line fit provides an average Q_0. (b) Pulse width data, τ, after removal of source pulse width. Reduction of variance mentioned in Figure 7 is apparent.

Tomographic Inversion

The Q inversion (Figs. 11 and 12) is based on rays traced in a 3D velocity model derived from travel-time tomography (Lees, 1995, unpublished results). The target volume is divided into 26 by 24 by 12 blocks each with 0.5-km horizontal extent and variable depth spacing taken from the 1D model used for hypocenter location. Model smoothing is achieved by constraining the Laplacian to be small (Lees and Crosson, 1989). The Q inversion (or, explicitly, C/Q) reduced data variance (observed minus predicted) by 80.1% and yielded a model that balanced the compromise between variance reduction and smoothness based on *a priori* assumptions regarding expected wavelengths of
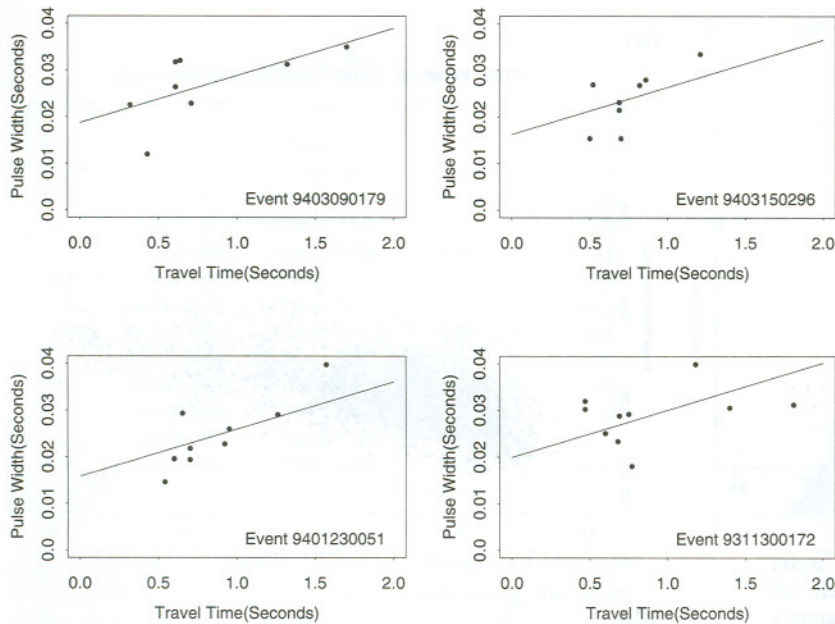
Figure 10. Pulse widths versus travel time for four sample events. Slopes of straight line fits are fixed to be $C/Q_0 = 0.01013086$ estimated from data described in Figure 9. The intercepts of the straight line fits are estimates of the initial source pulse width, τ_0.

anomalies. The average dominant frequency content of P-wave arrivals is about 50 Hz. Using $V_p = 5$ km/sec, the first Fresnel zone radius is 0.025 km (1/4 of the wavelength), considerably smaller than blocks used in the tomographic inversion. The average Q/C of the resultant model is 91.23, consistent with $Q_0/C = 97.7$ estimated above.

Three-dimensional images are presented as layers in Figs. 11 and 12 where blocks with fewer than six penetrating rays are excluded. The Jackknife method (Lees and Crosson, 1989) was used to estimate Q model errors. Error estimates for depths of 0.5 to 3.6 km, based on 100 partitions of the data, were computed (Fig. 13). The errors in C/Q are largest at the edge of the resolved model, while at the center of the model, the errors are small. At station S1 for depths of 1.2 to 2.4 km, the estimated error in C/Q is ~9.1%. We thus concentrate on the interpretation of the central part of the model and discount results near the edges.

Layers 1 and 2 (depths of 0.0 to 0.150 km) do not provide much lateral information on Q variations because rays are primarily vertical, although a central low Q at Devil's Kitchen and Nicol Prospects is observed. Layer 3, depths of 0.150 to 0.310 km, appears to correlate well with surface geology: rhyolite domes generally exhibit lower Q, and a broad low Q area includes Devil's Kitchen and Coso Hot Springs. Layer 3 also correlates well with heat flow data measured at several hundred meters depth (Fig. 14d). From depths of 0.31 to 0.52 km (layer 4), there is a low Q area to the north corresponding to a broad, rhyolite field (Qrp, in Duffield and Bacon, 1981). Lower Q in this region may represent high temperature and fracture associated with emplacement of young rhyolite bodies (0.057 my, Qr, in Duffield and Bacon, 1981). There is also a low Q to the southwest that correlates well with elevated temperature and

heat flow contours at deeper depth (Fig. 14d). Low Q is centralized at Devil's Kitchen and Nicol Prospects.

The zone between 0.52 and 1.22 km (layer 5, Figs. 11d and 11g) is the lowest depth of most of Coso's geothermal production wells. There is a broad, low Q region in the center of the field that trends approximately ENE–WSW along Devil's Kitchen, Nicol Prospects, and Coso Hot Springs. The lowest Q at this level is found at Coso Hot Springs, and the extensive distribution of low Q suggests intrusion of magma below this region: Pleistocene rhyolites may have a common source close to Coso Hot Springs (Duffield and Bacon, 1981). The high Q region adjacent to Sugarloaf mountain may indicate that the intrusion core of the Sugarloaf Rhyolite dome is not significantly fractured. Low Q is observed around the assumed core of the intrusion since these rocks are highly fractured and thermally altered during the intrusion. From depths of 1.22 to 2.44 km (layer 6, Figs. 11e and 11h), a low Q region is seen to the north and south of the region. The low Q body below Coso Hot Springs and Devil's Kitchen extends into this layer. The high Q on the eastern side of the model may represent unintruded Mesozoic basement rock, which is presumably cooler and/or less fractured.

The deepest controlled layer in the model, layer 7 (2.44 to 3.66 km in depth, shown in Fig. 11f), shows a large low Q region centered at about 2 to 4 km southeast of Devil's Kitchen and Nicol Prospects where $Q = 30$, given $C = 0.5$. This may represent the top of a deeper magmatic body which supplies heat to observed anomalies at the surface and is consistent with other seismic studies in the area suggesting a crustal magma body between 5 and 20 km depths (Young and Ward, 1980; Walter and Weaver, 1980). Lower-resolution seismic studies previously identified a high-attenuation anomaly between depths of 3 and 5 km in this area (Ho-
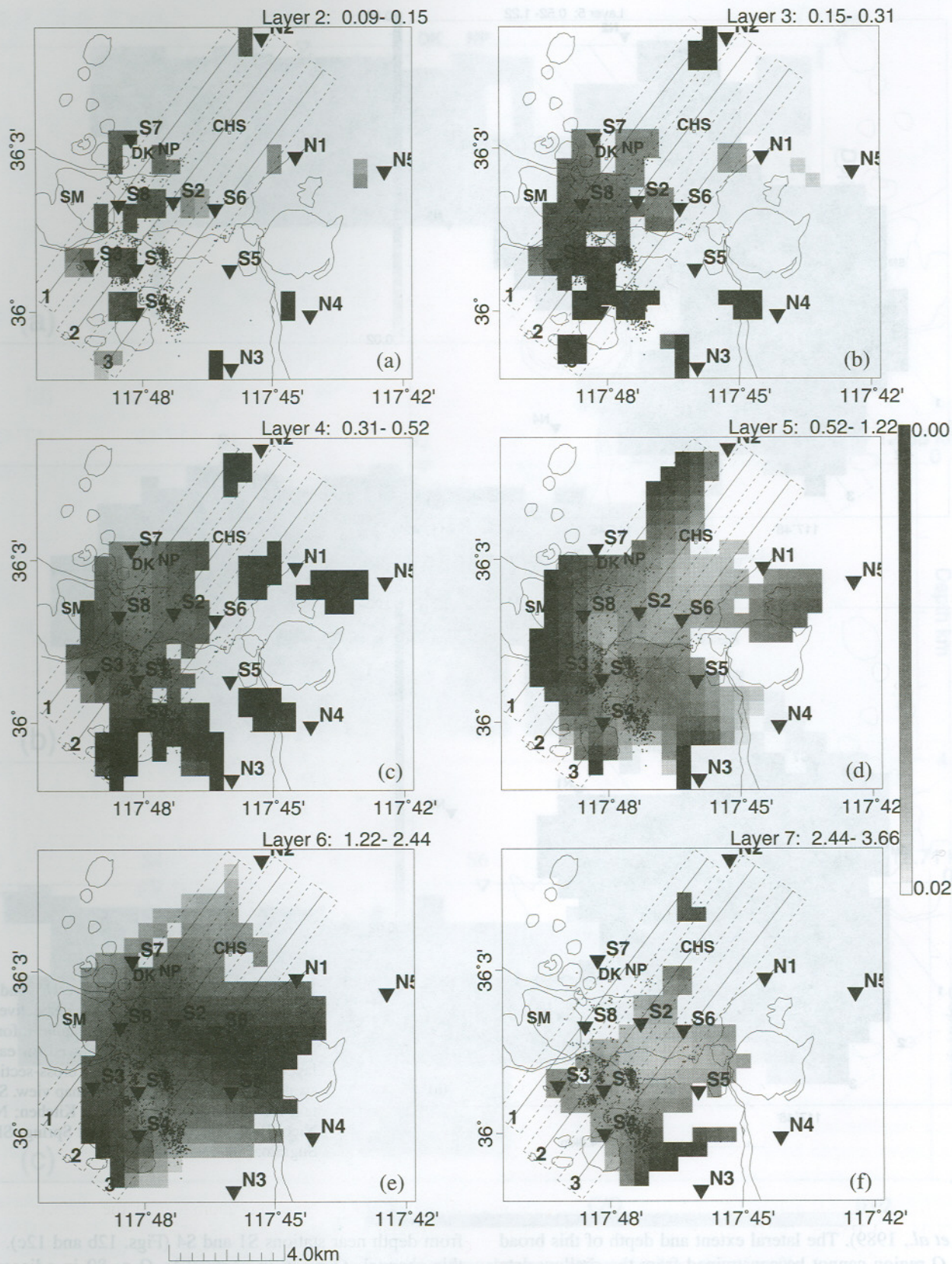
Figure 11. Tomographic inversion for *C/Q*. Blocks with fewer than six rays are blanked out. Dark areas have high *Q* (small *C/Q*), and light areas are those of low *Q* (large *C/Q*). (a) through (f) represent layers 2 through 7. (*continued on next page*)
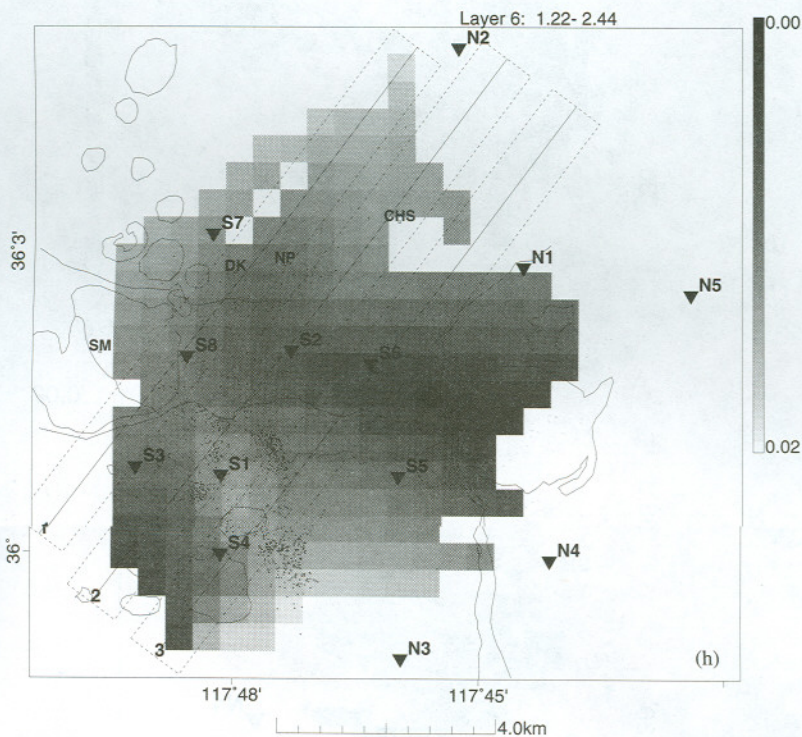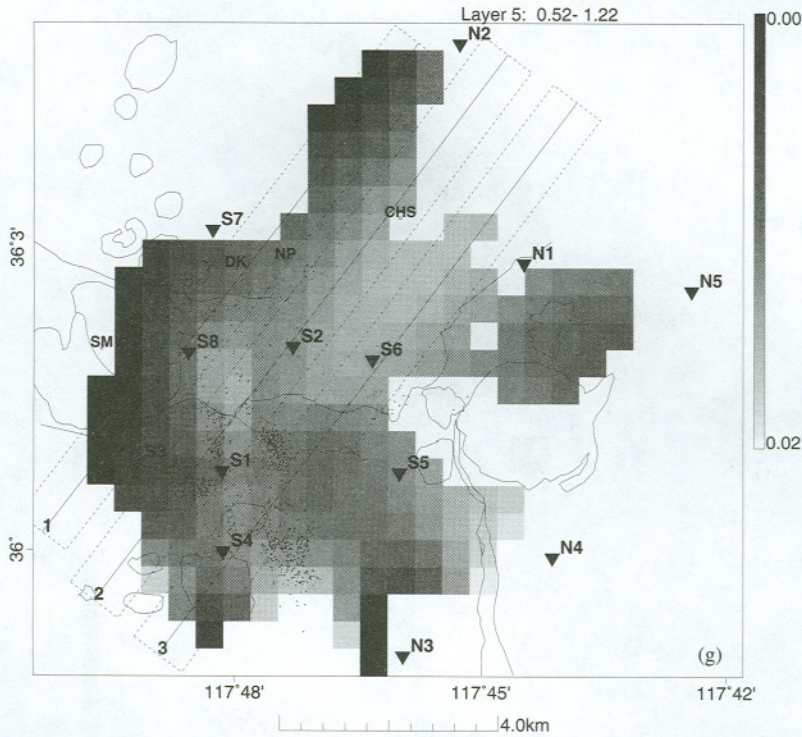
Layer 5: 0.52- 1.22

(g)

4.0km

Layer 6: 1.22- 2.44

(h)

4.0km

Figure 11. (*Continued*). Layers 5 and 6 are shown enlarged in (g) and (h), respectively. Stations, earthquakes, and geographic information from Figure 1 are displayed on each layer for reference. Vertical cross-section swaths 1, 2, and 3 are plotted in map view. See text for discussion. DK, Devil's Kitchen; NP, Nicol Prospects; CHS, Coso Hot Spring; SM, Sugarloaf mountain.

Liu *et al.,* 1989). The lateral extent and depth of this broad low Q region cannot be constrained from the shallow data used in our study.

In cross section (Fig. 12), the most prominent feature is a low Q channel, approximately 1 km in diameter, extending from depth near stations S1 and S4 (Figs. 12b and 12c). In this channel, $Q \approx 36$ in contrast to $Q \approx 80$ in adjacent, surrounding rocks with $C = 0.5$. Seismic scattering analysis suggests that a strong scattering body is located in this zone (Wu and Lees, 1995). At depths of 0.5 to 1.2 km, the channel
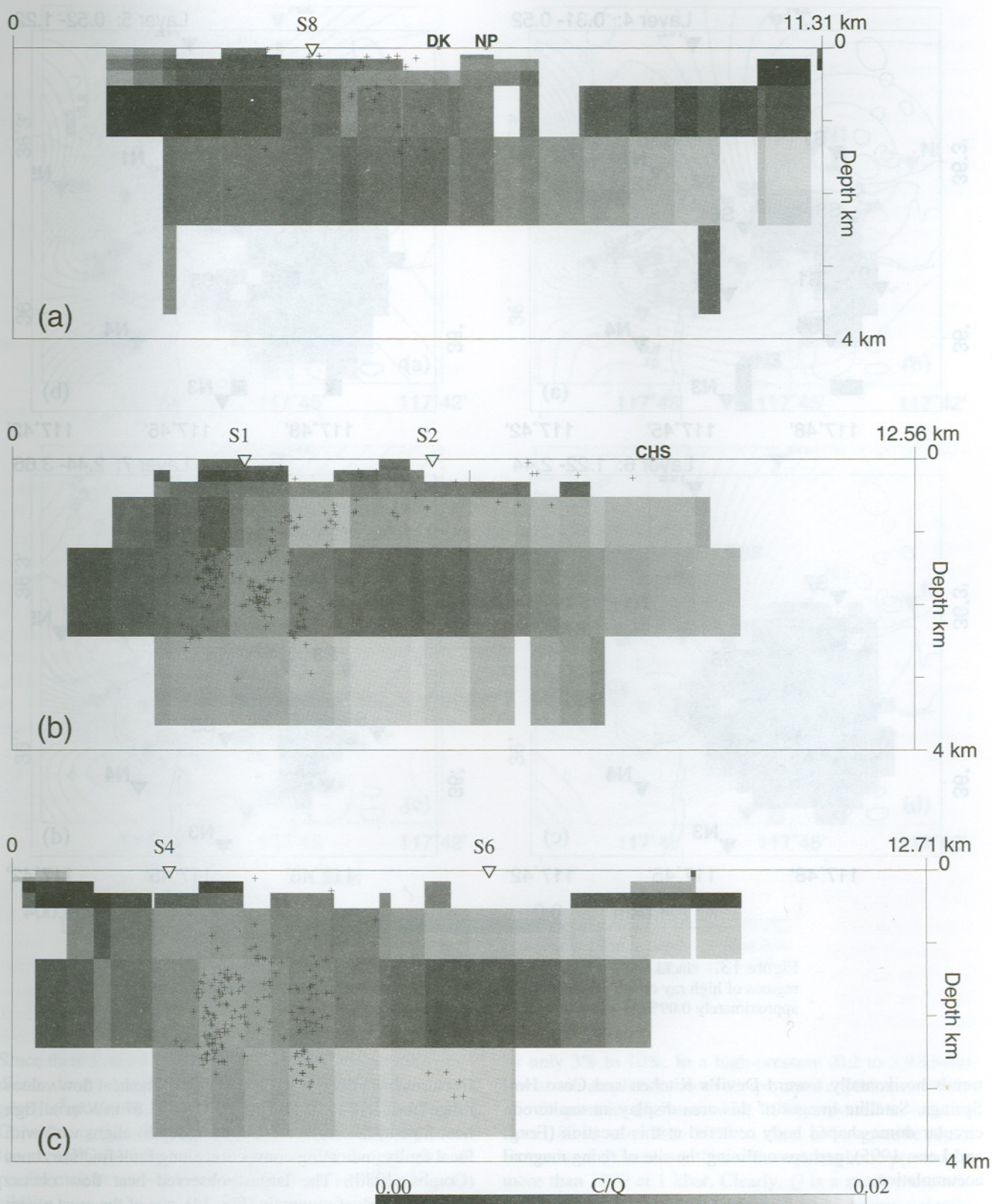
Figure 12.   Vertical cross sections through tomographic model. Map view of profile paths are presented in Figure 11(g). (a), (b), and (c) correspond to 1, 2, and 3, respectively. Note the concentrated high attenuation near stations S1 and S4 in sections (b) and (c).
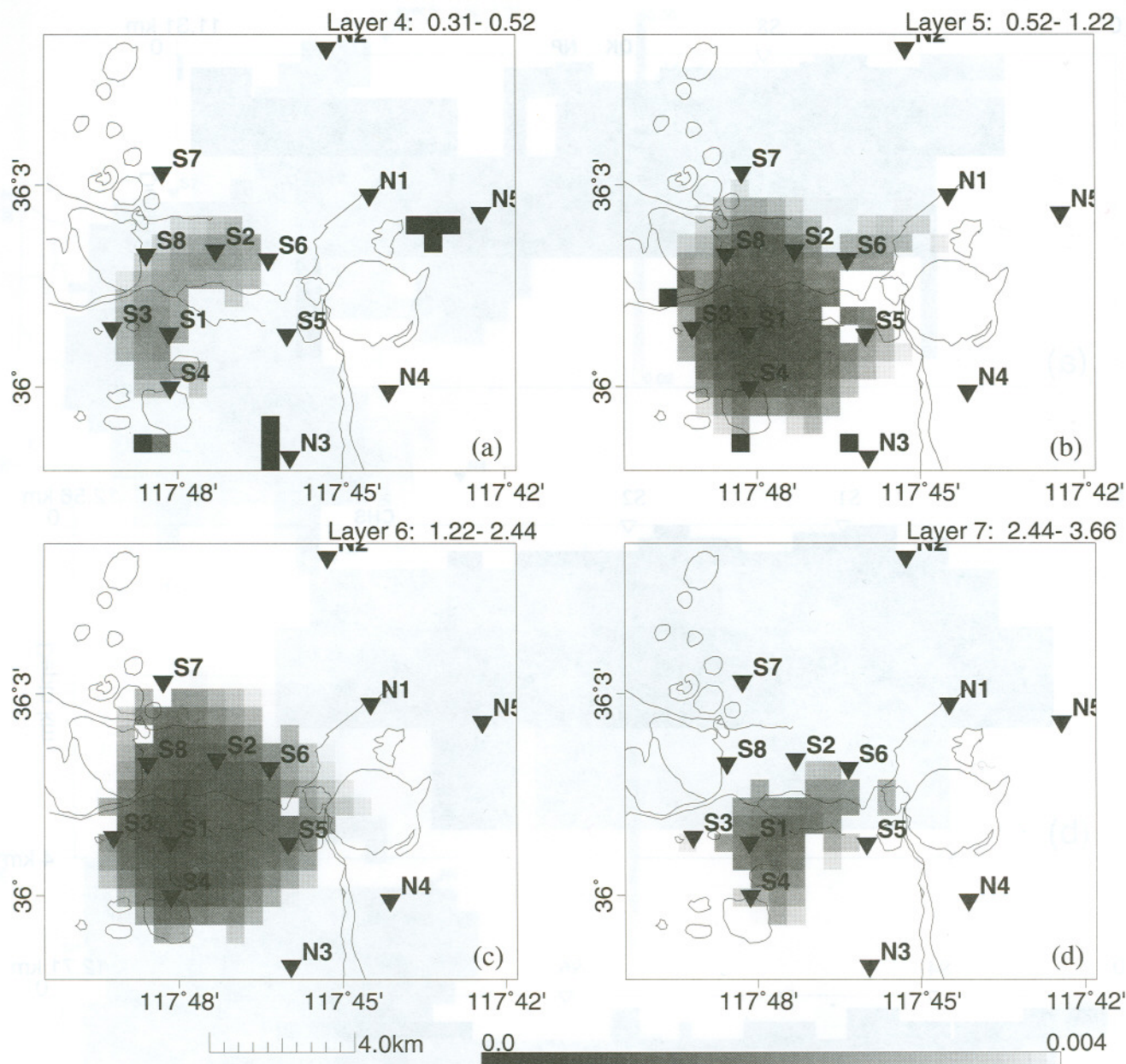
Figure 13.   Jackknife estimates of model errors. The smallest errors occur in the regions of high ray coverage. Below station S1 at 1.22 km in depth, the model error is approximately 0.09%.

trends horizontally toward Devil's Kitchen and Coso Hot Springs. Satellite images of this area display an unaltered, circular dome-shaped body centered at this location (Feng and Lees, 1995), perhaps outlining the site of rising magma accumulation.

Discussion

Temperature gradients at Coso range from 25.3°C/km to 905°C/km (Combs, 1980). These are mainly due to convective heat transport by high-temperature fluids through fractures from deep to shallow regions. The heat flow values range from 1.16 to 23 HFU (1 HFU = 41.87 mW/m^2). High heat flow at the surface (<35 m in depth) aligns well with local faults, indicating convection along fault fracture zones (Combs, 1980). The largest observed heat flow occurs around Sugarloaf mountain (Fig. 14), one of the most recent rhyolite domes, and Devil's Kitchen, a highly fumarolic area. Generally, we expect low Q to correlate with high temperature and/or high fracture.

Very high surface heat flow and temperature gradients (Fig. 14) have been reported in the Coso area (Combs, 1980).
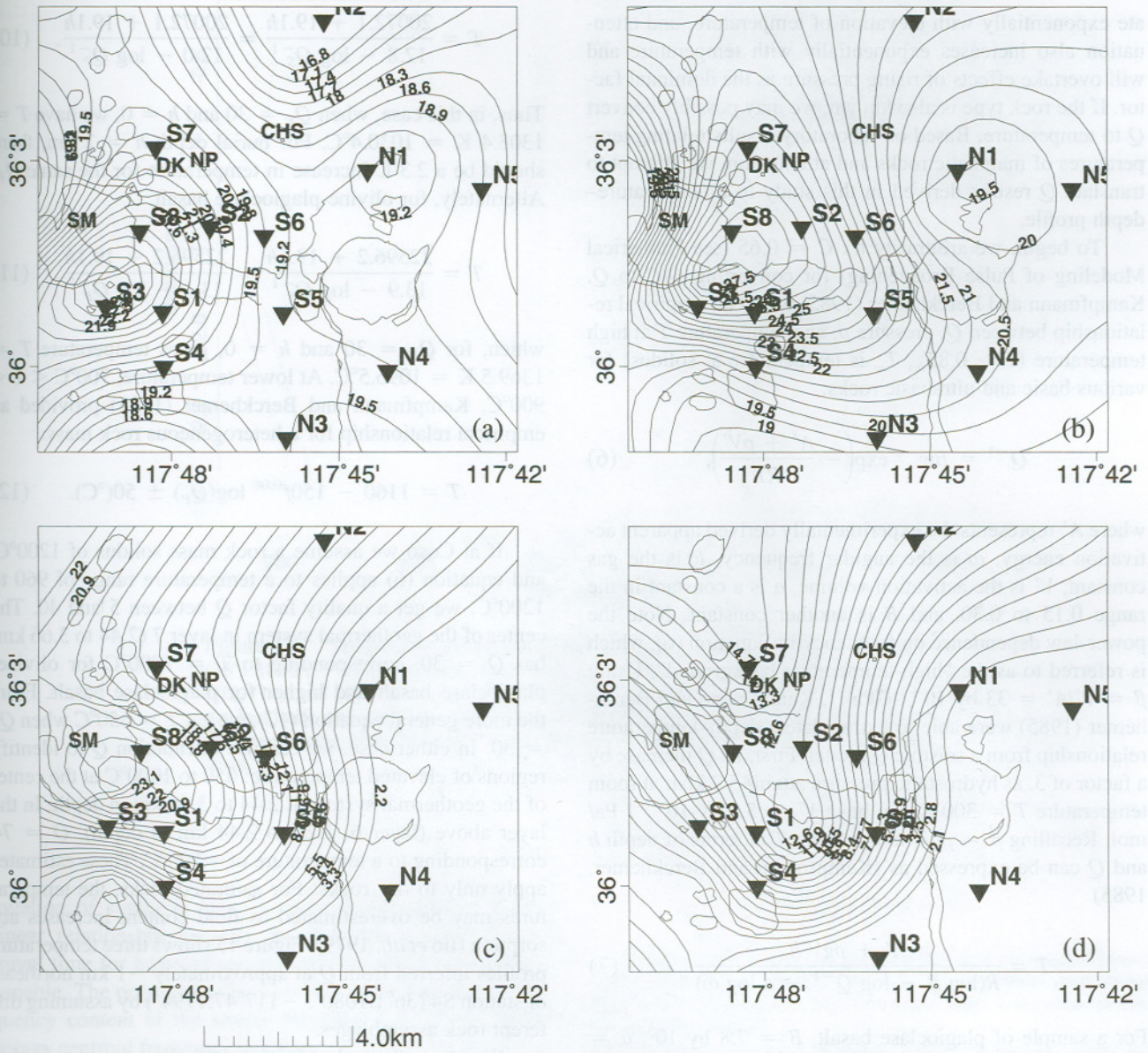
Figure 14. Borehole temperature and heat flow measurements. (a) Temperature (°C) contour at 5 m in depth. (b) Temperature (°C) contour at 10 m in depth. (c) Heat flow (HFU) contour for 15 to 65 m in depth. (d) Heat flow (HFU) contour for 35 to 135 m in depth [after Figs. 9, 10, and 11 of Combs (1980)].

Since there is nothing to suggest that these temperature gradients do not continue at depth, simple extrapolation suggests temperatures of up to 2000°C at 3 to 4 km in depth. Considering that some basaltic rocks become partially molten at 800°C (Murase and McBirney, 1973), the presence of partial melt at several kilometers in depth is a distinct possibility.

Experimental evidence indicates that Q, for common rocks under hydrostatic pressure, tends to rise with pressure (Ramara and Rao, 1974). A factor of 3 to 4 increase in Q is observed at room temperature when rocks are subjected to pressures up to 5.12 kbars, while seismic velocity increases

by only 3% to 10%. In a high-pressure (0.2 to 3.9 kbars), low-strain amplitude, room-temperature experiment at seismic frequencies (Jackson *et al.,* 1984) reported an increase from 180 to more than 1000 in shear Q for granitic rocks. Extensional Q increased from 70 at atmospheric pressure to more than 1000 at 1 kbar. Clearly, Q is a much more sensitive indicator of ambient pressure than seismic velocity. Given that hydrostatic pressure in the Earth is approximately ρgh and that rock density near the surface is approximately 3000 kg/m^3, hydrostatic pressure will increase at 0.3 kbar/km. At 3 km depth, then, we expect Q to double. On the other hand, dislocation (internal friction) processes acceler-

ate exponentially with elevation of temperature, and attenuation also increases exponentially with temperature and will overtake effects of rising pressure as the dominant factor. If the rock type is also known, we may possibly convert Q to temperature. Based on laboratory results relating temperatures of magmatic rocks and attenuation, we attempt to translate Q results derived in this study to a temperature–depth profile.

To begin, we arbitrarily fix $C = 0.65$ (see Numerical Modeling of Pulse Broadening) for converting Q/C to Q. Kampfmann and Berckhemer (1985) found an empirical relationship between Q, pressure p, and temperature T at high temperature ($T > 0.8T_m$, T_m is temperature at solidus) for various basic and ultrabasic rocks:

$$Q^{-1} = Bw^{-a}\exp\left(-\frac{A' + pV'}{RT}\right), \quad (6)$$

where A' represents the experimentally derived apparent activation energy, ω is the angular frequency, R is the gas constant, V' is the activation volume, a is a constant in the range 0.15 to 0.30, and B is another constant. Note the power-law dependence on frequency in Equation (6), which is referred to as the "high-temperature background". Using $\beta = V'/A' = 33$ by 10^{-3} GPa^{-1}, Kampfmann and Berckhemer (1985) were able to extrapolate a depth–temperature relationship from a seismic Q model. First, let Q increase by a factor of 3, as hydrostatic pressure attains 5.2 kbar at room temperature $T = 300$ K, we have $V' = 5.3$ by 10^{-6} J Pa/mol. Recalling $p = \rho g h$, temperature T in terms of depth h and Q can be expressed as (Kampfmann and Berckhemer, 1985)

$$T = \frac{A' + \rho g V' h}{R(\log B - \log Q^{-1} - a\log \omega)}. \quad (7)$$

For a sample of plagioclase basalt, $B = 7.8$ by 10^5, $a = 0.19 \pm 0.03$, $A' = 167 \pm 8$ kJ/mol, and for olivine-plagioclase basalt, $B = 3.3$ by 10^6, $a = 0.22 \pm 0.02$, $A' = 188 \pm 8$ kJ/mol. (In the laboratory experiments, torsion was used to deform rock samples, so all Q results are for shear waves.) Based on simple assumptions (Kampfmann and Berckhemer, 1985), a relationship between Q for P and S waves, with Poisson ratio $\nu = 0.25 \sim 0.3$, can be derived:

$$Q_P = (2.2 \approx 2.6)Q_S. \quad (8)$$

Since usually $\log B \gg a\log \omega$ for seismic frequencies 0.1 to 100 Hz, we may omit the frequency-dependent term and use instead a reference frequency of $f = 10$ Hz. By assuming $\rho = 3000$ kg/m^3,

$$T = \frac{A' + 159h}{R(\log B - \log Q^{-1} - 4.1a)}, \quad (9)$$

so, for plagioclase basalt, we have

$$T = \frac{20072.1 + 19.1h}{12.8 - \log Q_S^{-1}} = \frac{20072.1 + 19.1h}{12.0 - \log Q_P^{-1}}. \quad (10)$$

Thus, in this case, when $Q_P = 30$ and $h = 0$, we have $T = 1303.4$ K $= 1030.4$°C. For burial depth $h = 2$ km, there should be a 2.3°C increase in temperature for the same Q_P. Alternately, for olivine-plagioclase basalt,

$$T = \frac{22596.2 + 19.1h}{13.9 - \log Q_S^{-1}} = \frac{22596.2 + 19.1h}{13.1 - \log Q_P^{-1}}, \quad (11)$$

which, for $Q_P = 30$ and $h = 0$, gives temperature $T = 1369.5$ K $= 1096.5$°C. At lower temperature, 700°C $< T <$ 900°C, Kampfmann and Berckhemer (1985) provided an empirical relationship for a heterogeneous rock mass:

$$T = 1160 - 150f^{0.06}\log(Q_P) \pm 50(°C). \quad (12)$$

If at Coso we assume a rock mass solidus of 1200°C, and equation (6) applies to a temperature range of 960 to 1200°C, we get a quality factor Q between 5 and 40. The center of the geothermal system in layer 7 (2.44 to 3.66 km) has $Q = 30$, corresponding to $T = 1000$°C for olivine-plagioclase basalt and higher for plagioclase basalt. From the more general equation (12), we get $T = 650$°C when $Q_P = 30$. In either case, we can use attenuation Q to identify regions of elevated temperature: 650 to 1000°C at the center of the geothermal system at 2.44 to 3.66 km in depth. In the layer above (layer 6, 1.22 to 2.44 km in depth), $Q = 74$ corresponding to a temperature of ≈ 500°C. These estimates apply only to dry rocks: For saturated rocks, the temperatures may be overestimated as fluid content increases absorption (Ito *et al.*, 1979). Figure 15 shows three temperature profiles inferred from Q at approximately ~ 1 km northeast of station S4 (36°1.1080′, $-117°47.1794′$) by assuming different rock assemblages.

We stress that other factors, including fractures, lithologic variations, and fluid saturation, can lower Q in real situations, and we should not simply assume that all variations in Q are due to temperature fluctuations. Our estimate may, thus, be considered an upper bound on subsurface temperatures for dry rocks without fracture and convection. Bounds of these sorts are commonly used to delineate magma accumulations in volcanic areas, where the presence (or absence) of seismicity is used as evidence that the temperature is either well above or below the liquidus point (Iyer, 1992; Sanders *et al.*, 1995).

Conclusions

In this study, we have assumed that pulse width broadening is linearly related to Q^{-1} and that microseismic sources are impulses, or nearly so. When the second assumption is invalid, we can still derive an inversion for relative Q/C rather than absolute Q. Through numerical cal
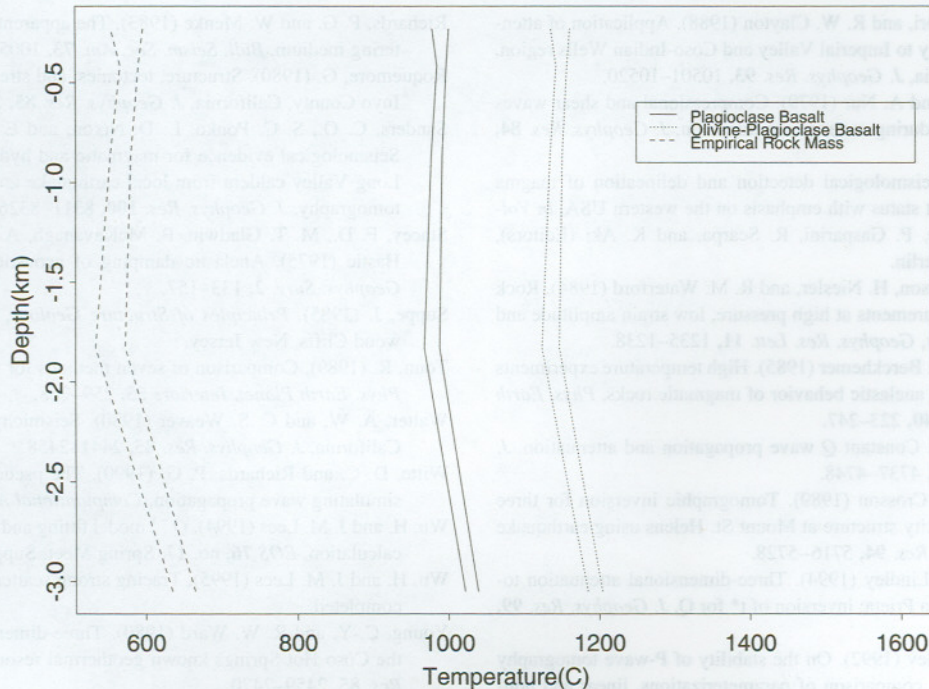
Figure 15. Temperature profile converted from Q at ~1 km northeast of station S4 (36°1.1080′, −117°47.1794′). The temperature is computed by empirical relations (10), (11), and (12). Two curves are plotted for each assumed rock mass, bracketed by the Jackknife estimated errors (Fig. 13). Solid lines represent plagioclase basalt, dotted lines are olivine-plagioclase basalt, and dashed lines are for an empirical average rock mass.

culation of synthetic seismograms, we established that a linear relationship between pulse width broadening and travel time for heterogeneous structures with cracks is reasonable. The proportionality constant C depends on the frequency content of the source function. By computing the energy centroid frequency in successive time windows along the P-wave train, intrinsic absorption, as opposed to scattering, appears to be the dominant attenuation factor in the Coso field, at least in the upper 4 km.

The average Q in the Coso geothermal area is estimated to be ~49. A broad region of low Q (30 to 37) has been identified at 0.5 to 1.2 km in depth below Devil's Kitchen, Nicol Prospects, and Coso Hot Springs. Based on three-dimensional Q analysis, another larger, deeper (2.5 to 3.6 km) low Q feature is observed 2 to 3 km southeast of Devil's Kitchen and Nicol Prospects and is probably the main origin of hydrothermal energy at Coso. This feature is related to a suspected rising magma accumulation, although the vertical extent of the presumed magma body is not constrained by the current data set. A vertical, low Q channel about 1 km in width connecting these two shallow regions of low Q is identified southwest of Devil's Kitchen and Nicol Prospects and may be the main conduit supplying geothermal energy to the surface.

Acknowledgments

References

Aki, K. and P. G. Richards (1980). *Quantitative Seismology: Theory and Methods,* W. H. Freeman and Company, New York.

Blair, D. P. and A. T. Spathis (1982). Attenuation of explosion-generated pulse in rock mass, *J. Geophys. Res.* **87,** 3885–3892.

Combs, J. (1980). Heat flow in the Coso geothermal area, Inyo County, California, *J. Geophys. Res.* **85,** 2411–2424.

Duffield, W. A. and C. R. Bacon (1981). Geologic map of the Coso volcanic field and adjacent areas, Inyo County, California, *U.S. Geol. Surv. Misc. Invest. Series MAP-1200.*

Duffield, W. A., C. R. Bacon, and G. B. Dalrymple (1980). Late Cenozoic volcanism, geochronology and structure of the Coso Range, Inyo County, California, *J. Geophys. Res.* **85,** 2381–2404.

Feng, Q. and J. M. Lees (1995). Application of landsat thematic mapper data at Coso, California, *EOS* **76,** no. 17, Spring Meet. Suppl., S193.

Gladwin, M. T. and F. D. Stacey (1974). Anelastic degradation of acoustic pulses in rock, *Phys. Earth Planet. Interiors* **8,** 332–336.

Ho-Liu, P., H. Kanamori, and R. W. Clayton (1988). Application of attenuation tomography to Imperial Valley and Coso-Indian Wells region, southern California, *J. Geophys. Res.* **93,** 10501–10520.

Ito, H., J. DeVilbiss, and A. Nur (1979). Compressional and shear waves in saturated rock during water-steam transition, *J. Geophys. Res.* **84,** 4731–4735.

Iyer, H. M. (1992). Seismological detection and delineation of magma chambers: present status with emphasis on the western USA, *in Volcanic Seismology,* P. Gasparini, R. Scarpa, and K. Aki (Editors), Spring-Verlag, Berlin.

Jackson, I., M. S. Paterson, H. Niesler, and R. M. Waterford (1984). Rock anelasticity measurements at high pressure, low strain amplitude and seismic frequency, *Geophys. Res. Lett.* **11,** 1235–1238.

Kampfmann, W. and H. Berckhemer (1985). High temperature experiments on the elastic and anelastic behavior of magmatic rocks, *Phys. Earth Planet. Interiors* **40,** 223–247.

Kjartansson, E. (1979). Constant Q wave propagation and attenuation, *J. Geophys. Res.* **84,** 4737–4748.

Lees, J. M. and R. S. Crosson (1989). Tomographic inversion for three dimensional velocity structure at Mount St. Helens using earthquake data, *J. Geophys. Res.* **94,** 5716–5728.

Lees, J. M. and G. T. Lindley (1994). Three-dimensional attenuation tomography at Loma Prieta: inversion of t* for Q, *J. Geophys. Res.* **99,** 6843–6863.

Lees, J. M. and E. Shalev (1992). On the stability of P-wave tomography at Loma Prieta: a comparison of parameterizations, linear and non-linear inversions, *Seism. Soc. Am. Bull.* **82,** 1821–1839.

Majer, E. L. and T. V. McEnvilly (1979). Seismological investigations of The Geysers geothermal field, *Geophysics* **44,** 246–269.

Murase, T. and A. R. McBirney (1973). Properties of some common igneous rocks and their melts at high temperatures, *Geol. Soc. Am. Bull.* **84,** 3563–3592.

Ramara, Y. V. and M. V. M. S. Rao (1974). Q by pulse broadening in rocks under pressure, *Phys. Earth Planet. Interiors* **8,** 337–341.

Reasenberg, P., W. Ellsworth, and A. Walter (1980). Teleseismic evidence for a low-velocity body under the Coso Geothermal Area, *J. Geophys. Res.* **85,** 2471–2483.

Richards, P. G. and W. Menke (1983). The apparent attenuation of a scattering medium, *Bull. Seism. Soc. Am.* **73,** 1005–1022.

Roquemore, G. (1980). Structure, tectonics, and stress of the Coso Range, Inyo County, California, *J. Geophys. Res.* **85,** 2434–2440.

Sanders, C. O., S. C. Ponko, L. D. Nixon, and E. A. Schwartz (1995). Seismological evidence for magmatic and hydrothermal structure in Long Valley caldera from local earthquake attenuation and velocity tomography, *J. Geophys. Res.* **100,** 8311–8326.

Stacey, F. D., M. T. Gladwin, B. McKavanagh, A. T. Linde, and L. M. Hastic (1975). Anelastic damping of acoustic and seismic pulses, *Geophys. Surv.* **2,** 133–157.

Suppe, J. (1985). *Principles of Structure Geology,* Prentice-Hall, Englewood Cliffs, New Jersey.

Tonn, R. (1989). Comparison of seven methods for the computation of Q, *Phys. Earth Planet. Interiors* **55,** 259–268.

Walter, A. W. and C. S. Weaver (1980). Seismicity of the Coso Range, California, *J. Geophys. Res.* **85,** 2441–2458.

Witte, D. C. and Richards, P. G. (1990). The pseudospectral method for simulating wave propagation, *Computational Acoustics* **3,** 1–18.

Wu, H. and J. M. Lees (1994). Q^{-1} model fitting and synthetic seismogram calculation, *EOS* **76,** no. 17, Spring Meet. Suppl., 227.

Wu, H. and J. M. Lees (1995). Tracing strong scatters in Coso, California, completed.

Young, C.-Y. and R. W. Ward (1980). Three-dimensional Q^{-1} model of the Coso Hot Springs known geothermal resource area, *J. Geophys. Res.* **85,** 2459–2470.

Zucca, J. J., L. J. Hutchings, and P. W. Kasameyer (1994). Seismic velocity and attenuation structure of the Geysers Geothermal Field, California, *Geothermics* **23,** 111–126.

Department of Geology and Geophysics
Yale University
210 Whitney Avenue
New Haven, Connecticut 06510